Int. J. Electrochem. Sci., 17 **(2022)** Article Number: 220746, doi: 10.20964/2022.07.49

International Journal of
ELECTROCHEMICAL
SCIENCE
www.electrochemsci.org

Influence of industrial robot trajectory on electrochemical machining quality

Lijun Jiang[1,3], *Ming Fang*[2,3*], *Yuanlong Chen*[1], *Fusheng Xia*[2], *Wei You*[3]

[1] School of Mechanical Engineering, Hefei University of Technology, Hefei 230009, China
[2] School of Mechanical Engineering, Anhui Polytechnic University, Wuhu 241000, China
[3] R&D Center, Efort Intelligent Equipment Co., Ltd, Wuhu, 241007, China
[*]E-mail: fangming@ahpu.edu.cn

Received: 2 April 2022 / *Accepted:* 9 May 2022 / *Published:* 6 June 2022

Industrial robots cannot move with the same precision as machine tools. In this research, a simulation method was introduced to study the influence of normal errors on material removal to reduce the impact of the motion accuracy of industrial robots on machining quality. Laser tracker measurement equipment was used to measure at the end of trajectory precision, which was converted into the normal motion of the cathode. A simulation method for electrochemical machining (ECM) process was introduced to study the influence of normal errors, processing voltages and X-axis moving speed on material removal. Experiments were conducted to illustrate the simulation method in robot ECM process. Results showed that the proposed method can effectively reflect the actual process.

Keywords: Electrochemical machining; Industrial robot; Trajectory error; Process simulation; Machining precision

1. INTRODUCTION

With the development of aerospace and other technologies, various new metal materials and new complex structures emerge one after another. Consequently, meeting the processing needs of these material parts becomes increasingly difficult for traditional machining methods. By virtue of its special advantages, electrochemical machining (ECM) technology has become a key manufacturing technology for complex structure and special metal material parts, which has achieved remarkable results [1, 2].

However, in ECM process, cathode design often follows the ‘trial and error’ approach, resulting in high development costs, especially the cathode design of complex structures. Many scholars began to study the simulation of ECM process. For instance, Kozak et al. used this model to study the rough machining of aero engine blades by DC electrolysis and finishing machining by pulse electrolysis [3]. Smets et al. established a simulation analysis model of temperature field based on the convection–diffusion equation and studied the evolution of temperature in pulse ECM. The study showed that when

the pulse was intermittent, the change in electrolyte temperature consisted of two parts: the rapid heat dissipation of the electrolyte by convection and the heating effect of the electrode on the electrolyte [4]. Smets et al. proposed a quasi-steady state simplified algorithm model to quickly solve the equilibrium temperature distribution of the system in the process of pulse ECM. The algorithm regards the average steady-state temperature as the initial state before pulse current is applied [5, 6].

A method of NC ECM has been proposed; that is, the complex cathode is replaced with the spreading motion of the cathode, which avoids the design and manufacture of a complex forming cathode [7]. An external nozzle was used to spray an electrolyte on the surface of a stainless steel workpiece, and the study of groove smoothness in electrolytic milling was carried out by Hinduja and Pattavanitch [8]. A tubular electrode with an outer diameter of 7 mm and an inner diameter of 6 mm was used for macroscopic electrochemical milling when machining the plane [9]. The surface of GH4169 alloy was electrolytically milled to produce a plane of high quality, and the same tool electrode span ratio and annular cutting mode were used to produce a plane structure on the surface of TB6 titanium alloy. The quality of GH4169 alloy was very different from that of TB6 titanium alloy [10].

Although professional CNC machine tools have high motion accuracy and production efficiency, disadvantages, such as high price, poor scalability and difficulty in meeting the demands of highly flexible machining, remain. Meanwhile, robotic ECM has the advantages of good flexibility, easy scheduling, strong versatility and low cost, which makes it increasingly applied in the processing of complex and difficult materials. However, the robot has some problems, such as low motion accuracy and insufficient rigidity, which greatly affect the accuracy of ECM and thus limit its application.

The positioning error prediction and compensation methods of industrial robots include joint space compensation [11], error compensation based on interpolation thinking and error compensation based on neural network. Angelidis et al. measured the trajectory of an industrial robot at a specific point position error by using an artificial neural network to establish a forecast model of industrial robot positioning error, the differences in the working space positioning error of the industrial robot was forecasted, and the neural network was constructed on the basis of the minimum error to calculate the coordinates of each joint of the industrial robot. The industrial robot was controlled by compensation [12]. Considering the influence of joint error on a robot's multidirection, Zhang et al. installed a grating ruler on the front three-axis joints of KUKA KR210 and used the Chebyshev polynomial to carry out joint interpolation compensation, so that the hole-making accuracy reached 0.25 mm [13].

In this paper, an ECM method for industrial robots was proposed to solve the surface machining problems of complex and difficult machining materials. A simulation method was introduced to study the influence of normal errors, processing voltages and X-axis moving speed on material removal to reduce the impact of the motion accuracy of industrial robots on machining quality.

2. THEORETICAL MODEL

2.1 Kinematic error model of robot joints

Assembly manufacturing error of industrial robot ontology causes deviations in actual kinematic parameters and controller parameters. Furthermore, the weak stiffness characteristics of industrial robot joints are transmitted and amplified by mechanical arms, which affects the precision of robot ECM.

Defining joint vector parameters q and kinematic error Δq causes robot pose error $\Delta_T^B T$ by

$$\Delta_{\mathrm{T}}^{\mathrm{B}}\mathrm{T}_{\mathrm{q}} = {}_{\mathrm{T}}^{\mathrm{B}}\mathrm{T}(\mathrm{q}+\Delta\mathrm{q}) - {}_{\mathrm{T}}^{\mathrm{B}}\mathrm{T}(\mathrm{q}) \quad (1)$$

where {B} is the base coordinate system of the robot, {T} is the tool coordinate system, and ${}_T^B T$ is the pose of frame {T} with respect to frame {B}.

The pose error vector ${}^{P_i}D_q$, which is composed of position error ${}^{P_i}d_q = [{}^{P_i}d_x, {}^{P_i}d_y, {}^{P_i}d_z]$ and attitude error ${}^{P_i}\delta_q = [{}^{P_i}\delta_x, {}^{P_i}\delta_y, {}^{P_i}\delta_z]$, satisfies the adjoint transformation of velocity [14]:

$${}^{P_i}D_q = \begin{bmatrix} {}^{P_i}d_q \\ {}^{P_i}\delta_q \end{bmatrix}^T = \begin{bmatrix} {}_T^{P_i}R & \left[{}^{P_i}t_{To}\right]{}_T^{P_i}R \\ 0_{3\times3} & {}_T^{P_i}R \end{bmatrix} {}^{T}D_q = Ad_V\left({}_T^{P_i}T\right)\left({}_T^B T^{-1}(q)\left({}_T^B T(q+\Delta q) - {}_{\mathrm{T}}^{\mathrm{B}}\mathrm{T}(\mathrm{q})\right)\right)^{\vee} \quad (2)$$

where ${}^{T}D_q \in R^6$ represents the pose error vector of the tool coordinate system {T} caused by kinematic error, Ad_V is the velocity adjoint transformation operator, and ∨ represents an operator that converts a differential operator into a differential motion vector.

The ECM gap is related to the normal error. Therefore, the normal motion error expressed by point-section distance is [15]

$$\varepsilon_q(P_i) = {}^{P_i}d_z = \left({}^{P_i}D_q\right)^T D_z \quad (3)$$

where $\varepsilon_q(P_i)$ is the machining error of target point P_i, ${}^{P_i}d_z$ is the normal machining error of target point P_i, and ${}^{T}D_z$ is the pose error vector.

2.2 Relationship model between normal motion error and machining gap

During the pulse width time, the anode continuously dissolves, as shown in Fig. 1.

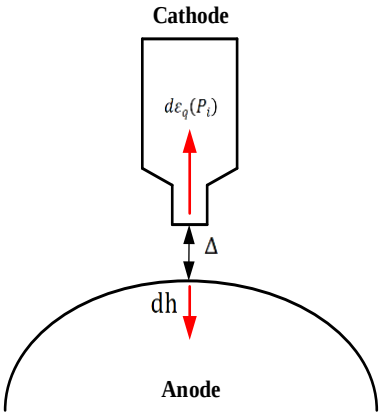

Figure 1. Schematic of the machining gap change.

The relationship between the normal motion error of tool cathode $d\varepsilon_q(P_i)$ and the variation in machining gap dΔ is [16]

$$\mathrm{d}\Delta = \upsilon_{\mathrm{a}}\mathrm{d}t + d\varepsilon_q(P_i) \quad (4)$$

where υ_{a} is the velocity of anodic dissolution.

During the pulse gap time, anodic dissolution stops. The relationship between $d\varepsilon_q(P_i)$ and dΔ is

$$\mathrm{d}\Delta = d\varepsilon_q(P_i) \quad (5)$$

Obtained from Equations (4) and (5), the variation in machining gap during one pulse period is

$$d\Delta = \upsilon_a D\tau + d\varepsilon_q(P_i) \quad (6)$$

where D is the duty cycle, and τ is the pulse period.

3. MODELLING OF ECM PROCESS FOR INDUSTRIAL ROBOTS

The geometric model of pulse ECM is shown in Fig. 2. The upper end of the cathode is connected to the negative pole of the pulse power supply, the lower end of the anode is connected to the positive pole of the pulse power supply, and the electrolyte has no flow. In the process of machining, the cathode moves uniformly from left to right. Due to the relatively low precision of robot motion, a motion error occurs in the normal direction of the cathode. In the simulation, the robot normal motion error is inserted into the model in the form of interpolation points as the normal direction of the cathode.

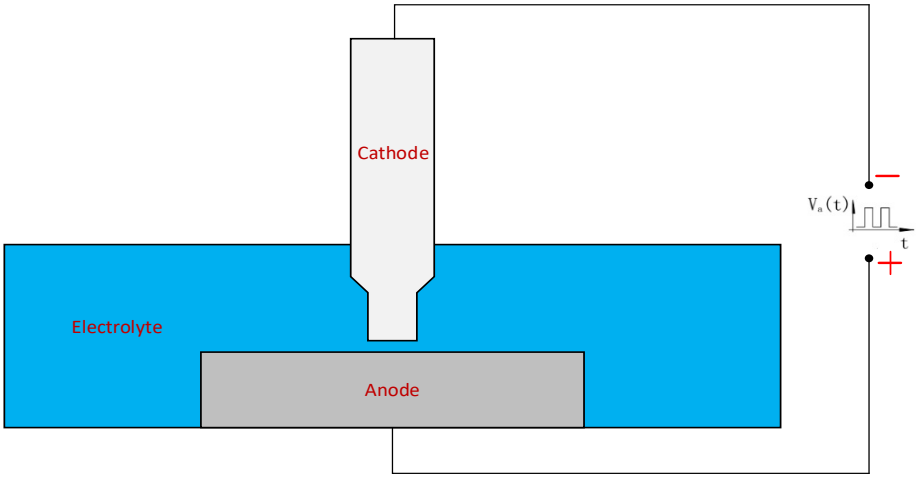

Figure 2. Geometric model of pulse ECM.

3.1 Electrical model

Assuming that the conductivity of the electrode is constant and the electrode material is isotropic, the potential distribution in the electrode satisfies the law of charge conservation [17]:

$$\nabla \cdot (\kappa_1 \nabla V) = 0 \quad (7)$$

where κ' is the electrode conductivity, and V is the potential distribution.

The solution of potential distribution *U* in the electrolyte is governed by the Laplace equation:

$$\nabla \cdot (\kappa \nabla U) = 0 \quad (8)$$

where κ is the electrolyte conductivity.

3.2 Material removal model

According to the first law of Faraday, the relationship between the actual anode metal dissolution rate and the local current density ***j*** is [18]

$$\upsilon_a = -\eta \frac{\vec{j}}{nF} \frac{M}{\rho} \qquad (9)$$

where n is the atomicity, F is the Faraday constant, M is the relative atomic mass, ρ is the density of the anode metal, and η is the current efficiency.

In the simulation of ECM process, the removal of anode material and the movement of tool cathode are realised by the movement and deformation of mesh. The ALE method is adopted, and the control function is a positive definite function matrix given on the domain, which is constructed as

$$f(\mathrm{X}_i, t) = g(\partial u / \partial l)\boldsymbol{I} \qquad (10)$$

The physical grid node corresponding to time t is denoted as $\mathbf{X}_{\mathrm{t}}^{\mathrm{i}}$, and the equations on the physical grid are solved by calculating the control function as

$$\frac{\partial}{\partial x^i}\left(f^{ij} \frac{\partial \xi^k}{\partial x^j} \right) = 0, \xi|_{\partial D_p} = \xi_b \qquad (11)$$

where D_p is the physical region.

The regional grid nodes are updated as

$$\mathrm{X}_{\mathrm{t:}} = \mathrm{X}_t^i + \sigma \cdot \delta X^{i,*} \qquad (12)$$

where σ is the moving step length of the grid, and $\delta X^{i,*}$ is the movement direction of the node.

4. ERROR MEASUREMENT AND SIMULATION STRATEGY

4.1 Accuracy measurement of robot trajectory

The workpiece coordinate system was defined, and the cathode posture at the end of the actuator was adjusted to be vertical with the anode surface. A measuring target ball was installed on the cathode flange. The measuring path was set for the parallel processing line on the anode surface. Leica AT930 laser tracker measurement equipment was used to measure at the end of trajectory precision, with a mining point frequency for 1000 damages per second. The measurement method was shown in the literature [19]. The relationship between theoretical trajectory and practical trajectory is shown in Fig. 3.

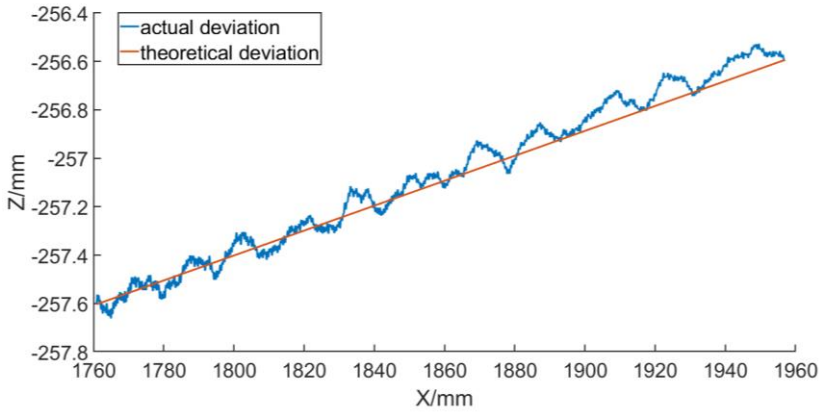

Figure 3. Errors of robot trajectory.

4.2 Simulation method and parameters

The normal motion of the cathode is caused by normal error of robot motion. Therefore, the Z-axis errors of robot trajectory were converted into the normal motion of the cathode[20]. The simulation procedure of ECM process is shown in Fig. 4.

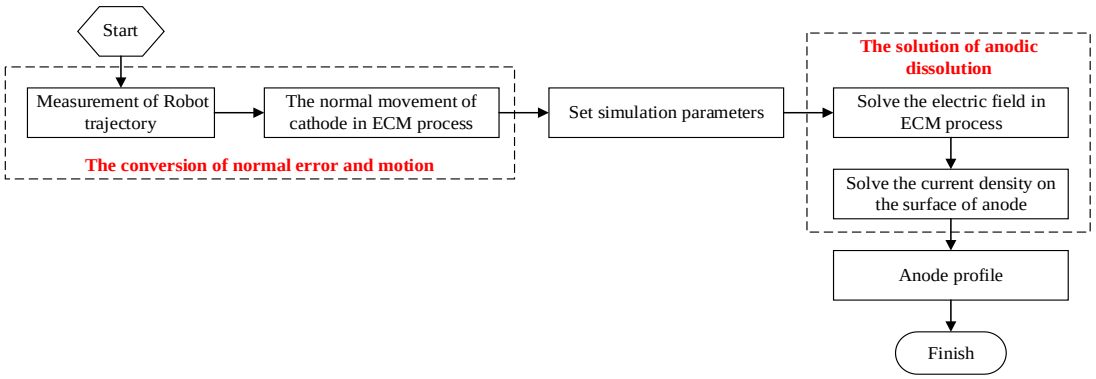

Figure 4. Simulation procedure of robot ECM process.

The following parameters were used for all simulations (unless stated otherwise). The processing parameters are shown in Table 1.

Table 1. Simulation parameters in robot ECM process.

Parameters	Value	Parameters	Value
Electrolyte conductivity	12.91 S/m	Temperature	25 ℃
Electrode conductivity	1.25×10^{6} S/m	Applied voltage	10 V
Pulse frequency	20 kHz	Pulse duty cycle	50%
Initial frontal gap	1.5 mm		

5. SIMULATION RESULTS

5.1 Influence of normal errors on material removal

The X-axis motion speed is 0.1 mm/s, and the remaining parameters are shown in Table 1. The current density distribution on the anode surface is solved under the conditions of normal errors and no normal errors.

Fig. 5 shows the current density distribution on the anode surface under the two conditions when the processing time is 20 s. The existence of normal error decreases the machining gap, increases the current density and aggravates the current density maldistribution in the corresponding processing zone at the cathode bottom[21]. The current density difference in the processing zone increases from 0.273 A/cm^2 in the absence of normal error to 0.538 A/cm^2 in the presence of normal error, which results in the production of machining errors.

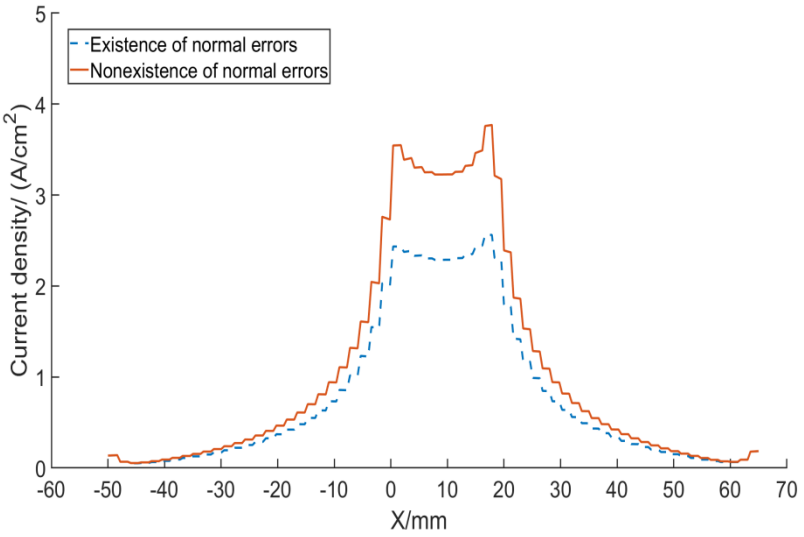

Figure 5. Distribution of current density on the anode surface.

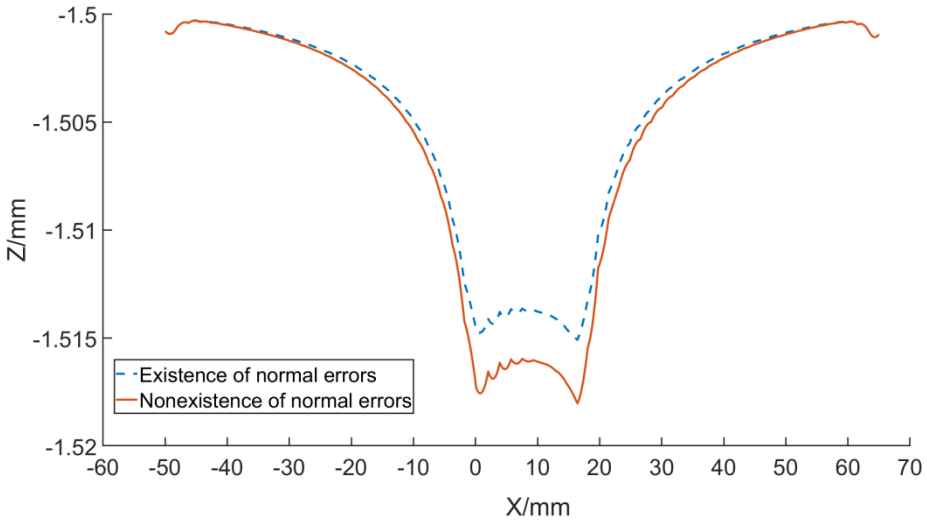

Figure 6. Anode profile under the conditions of normal errors and no normal errors.

Fig. 6 shows the anode profile under two conditions when the processing time is 20 s. The existence of normal error leads to a maximum increase in material removal of nearly 0.003 mm compared with the absence of normal error. For the machined surface, within the x-coordinate interval [0, 2], the unflatness of interval increases from 0.0006 mm when normal error does not exist to 0.001 mm.

5.2 Influence of processing voltages on material removal

Fig. 7 shows the influence of processing voltage on material removal under the condition of normal error with processing time of 20 s and X-axis moving speed of 0.1 mm/s. The greater the processing voltage is, the greater the material removal amount is. The material removal error caused by the normal errors gradually increases with the increase in the processing voltage[22]. The unflatness of interval increases from 0.0024 mm when the processing voltage is 6 V to 0.0047 mm when the processing voltage is 10 V.

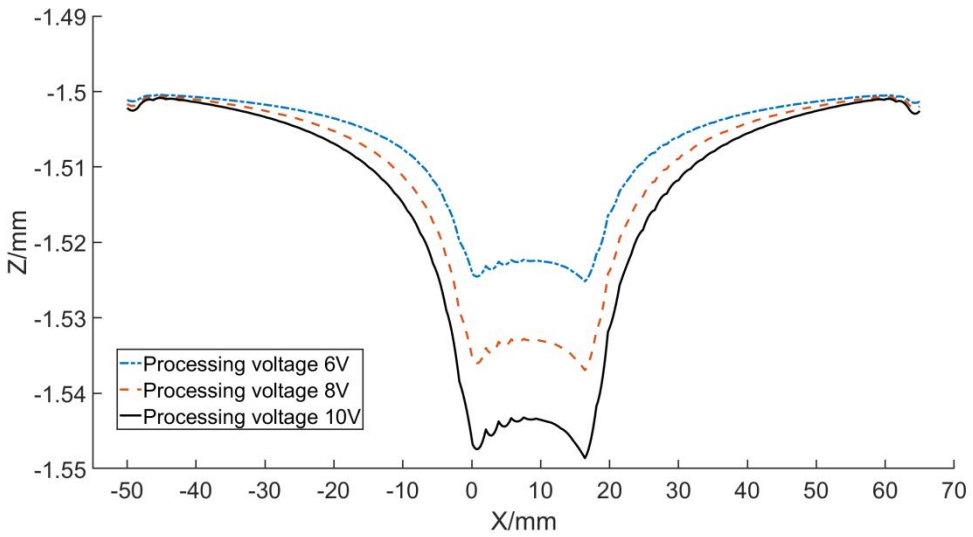

Figure 7. Changes in anode profile with processing voltages.

Fig. 8 shows the influence of processing voltages on the distribution of machining gap in the presence of normal errors. The machining gap increases gradually with the increase in processing voltage[23]. The distribution unevenness of machining gap increases from 0.0039 mm at 6 V to 0.0061 mm at 10 V.

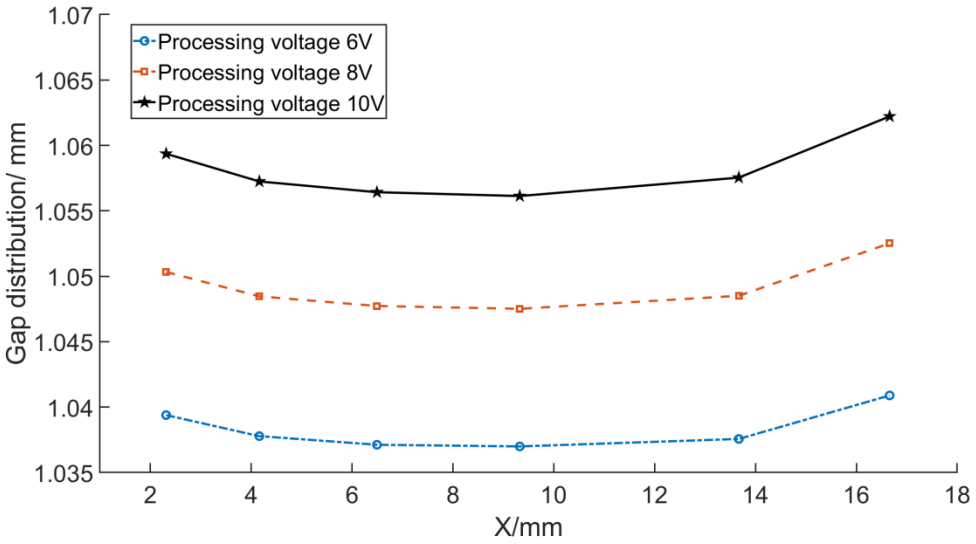

Figure 8. Changes in machining gap with processing voltages.

5.3 Influence of X-axis moving speed on material removal

Fig. 9 shows the influence of different X-axis moving speeds on the current density distribution on the anode surface under the condition of normal error at the machining voltage of 10 V. At the top of the distribution of current density, the higher the speed of movement on the left side is, the higher the current density value is. On the contrary, the faster the speed of movement on the right side is, the lower the current density value is, which is caused by the fact that at the top of the distribution, the left side is the processed surface, and the right side is the surface being processed[24]. In addition, the existence of normal error leads to unequal current density values on the left and right sides of the distribution top.

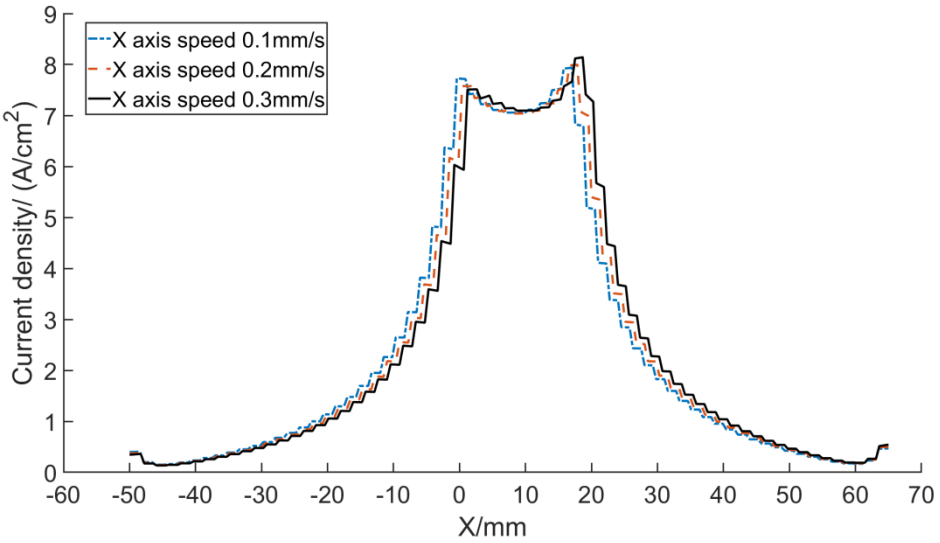

Figure 9. Changes in current density with X-axis moving speed.

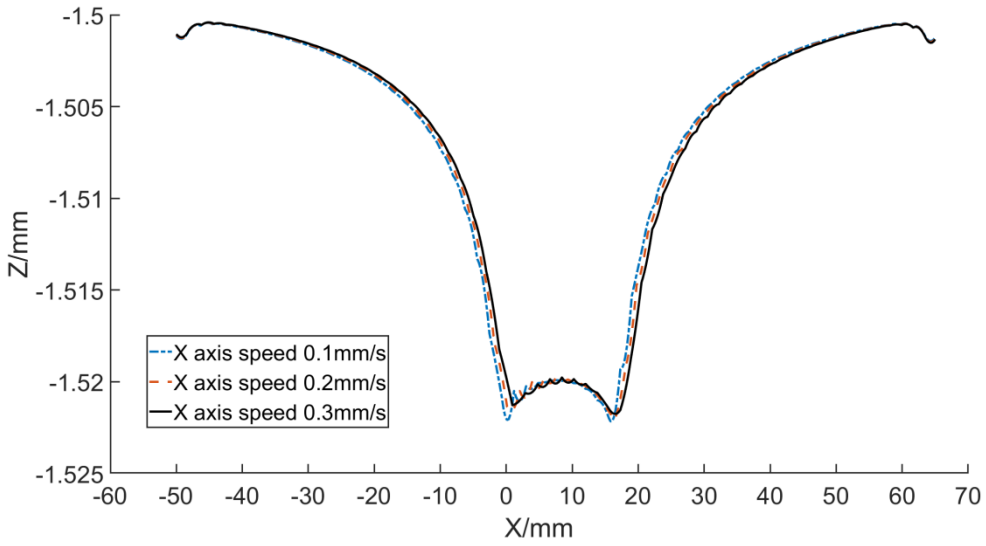

Figure 10. Changes in anode profiles with X-axis moving speed.

Fig. 10 shows the anode profiles at different moving speeds. At the bottom of the anode profiles, the unevenness gradually decreases with the increase in the movement velocity. The influence of normal errors is weakened with the increase in velocity.

6. EXPERIMENTAL VERIFICATION

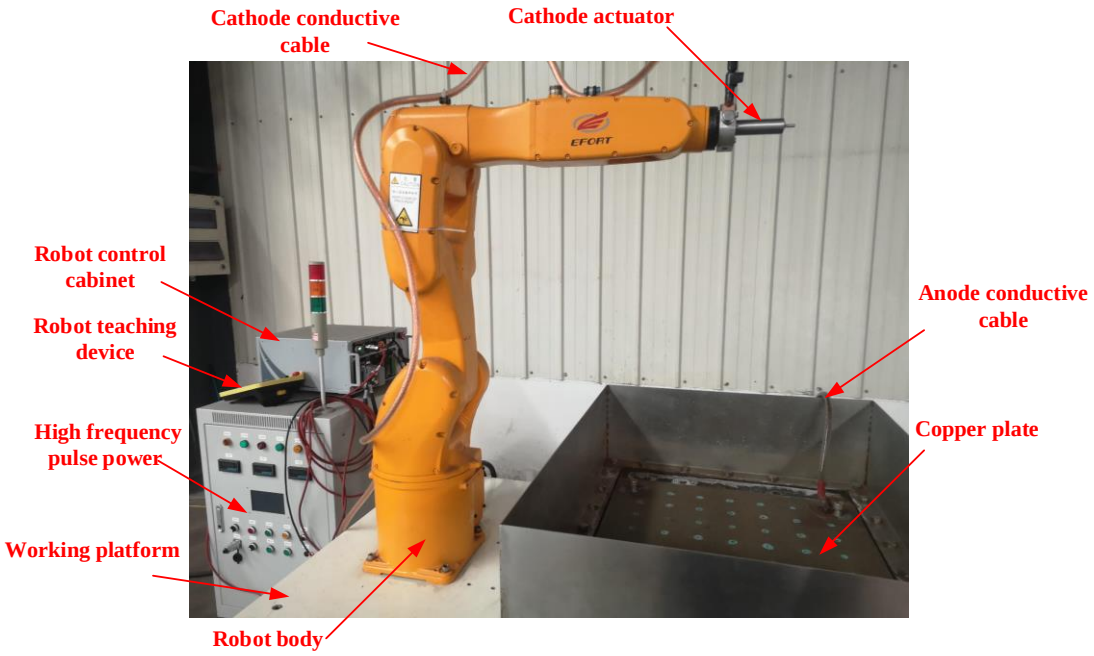

Figure 11. Platform of pulse ECM with an industrial robot.

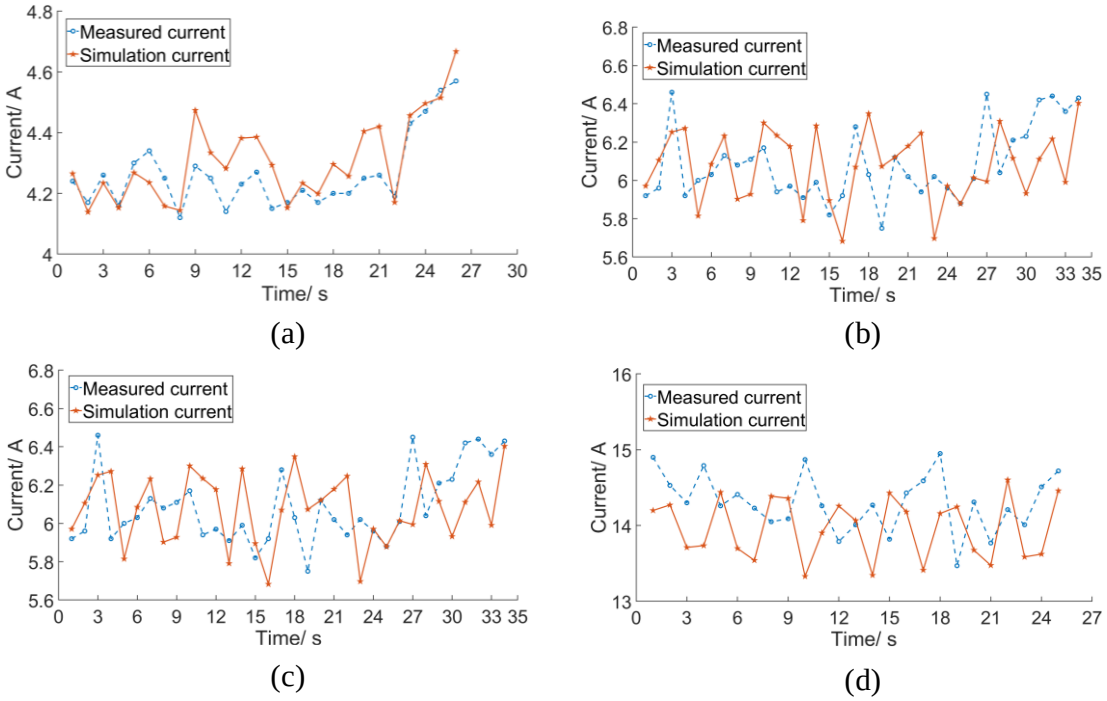

Figure 12. Comparison of measured and simulation currents under the voltages of 4.8 V (a), 6 V (b), 8 V (c) and 10 V (d).

To verify the effectiveness of the simulation model and method, an experimental platform of pulse ECM with an industrial robot was constructed. It was composed of robot body, robot control cabinet, high-frequency pulse power supply, robot installation platform, marble platform and conductive copper plate, as shown in Fig. 11.

The processing parameters in Table 1 were used as experimental parameters, and the X-axis movement velocity of the cathode was 5 mm/s. Experimental verification was carried out under the voltages of 4.8, 6, 8 and 10 V. The measured and simulation currents are shown in Fig. 12.

The maximum error between the measured and simulation currents was about 0.18 A under the voltage of 4.8 V, as shown in Fig. 12(a). With increasing voltages, the maximum error between the measured and simulation currents was increasing from 0.18 A under 4.8 V to 1.17 A under 10 V, as shown in Fig. 12. However, the simulation results could reflect the experimental results well in general.

7. CONCLUSION

An ECM method for industrial robots was proposed to solve the surface machining problems of complex and difficult machining materials. However, robots ’cannot move with the same precision as machine tools. Therefore, to reduce the impact of the motion accuracy of industrial robots on machining quality, a simulation method was introduced to study the influence of normal errors on material removal. Furthermore, the influences of processing voltages and X-axis moving speed on material removal were

studied. Experiments were conducted to verify the validity of the proposed method. The conclusions can be summarised as follows:

(1) The simulation results for the influence of normal errors on material removal indicated that the existence of normal error decreases the machining gap, increases the current density and aggravates the current density maldistribution in the corresponding processing zone at the cathode bottom.

(2) The simulation results for the effects of processing voltages and X-axis moving speed on material removal indicated that the material removal error caused by normal errors gradually increases with the increase in the processing voltage. At the top of the distribution of current density, the higher the speed of movement on the left side is, the higher the current density value is.

(3) The experimental results for verifying the proposed method indicated that the simulation results can reflect the experimental results well in general.

ACKNOWLEDGEMENTS
This work has been financially supported by the Natural Science Foundation of Anhui Province of China (2008085QE278), Science and Technology Planning Project of Wuhu City of China (2021jc1-5) and Key Research and Development Program of Anhui Province of China (202104h04020015).

References

1. K.P. Rajurkar, B. Wei, J. Kozak, *CIRP Ann. Manuf. Technol.,* 44 (1995) 177.
2. O. Weber, H. Natter, D. Bähre, *J. Solid State Electrochem.,* 19 (2015) 1265.
3. J. Kozak, *Proceedings of the World Congress on Engineering and Computer Science*, 2 (2013) 25.
4. N. Smets, S. Van Damme, D. De Wilde, G. Weyns and J. Deconinck, *J. Appl. Electrochem.*, 37 (2007) 324.
5. N. Smets, S. Van Damme, D. De Wilde, G. Weyns and J. Deconinck, *J. Appl. Electrochem.*, 37 (2007) 1355.
6. N. Smets, S. Van Damme, D. De Wilde, G. Weyns and J. Deconinck, *J. Appl. Electrochem.*, 38 (2008) 560.
7. J. Kozak, *J. Mater. Process Tech.,* 109 (2001) 354.
8. S. Hinduja, J. Pattavanitch, *CIRP J. Manuf. Sci. Tec.*, 12 (2016) 79.
9. W. Vanderauwera, M. Vanloffelt, R. Perez, B. Lauwers, *Procedia CIRP*, 6 (2013) 356.
10. X.D. Wang, N.S. Qu, P.F. Guo, X.L. Fang, X. Lin, *J. Electrochem. Soc.*, 164 (2017) 548.
11. W. Zhou, W.H. Liao, W. Tian. *Chin. Mech. Eng.*, 23 (2012) 2311.
12. A. Angelidis, G. Vosniakos. *Int. J. Precis. Eng. Man.*, 15 (2014) 73.
13. L. Zhang, W. Tian, F.Y. Zheng, et al., *Tran. NUAA*, 6 (2020) 871.
14. L.B. Da Silva, H. Yoshioka, H. Shinno, J. Zhu., *Int. J. Autom. Comput.*, 13 (2019) 582.
15. L. Wenlong, X. He, Y. Zhouping, D. Han, *J. Mech. Eng.*, 57 (2021) 154.
16. M. Fang, Y.L. Chen, L.J. Jiang, Y.S. Su, Y. Liang, *Int. J. Adv. Manuf. Technol.,* 105 (2019) 3270.
17. H. Lin, Y.L. Chen, X. Li, H.G. Li, Q. Chen, *Int. J. Electrochem. Sci.*, 16 (2021) 15.
18. Y.L. Chen, L.J. Jiang, M. Fang, J.C. Zhang, *Int. J. Adv. Manuf. Technol.,* 110 (2020) 2210.
19. H.N. Nguyen, J. Zhou, H.J. Kang, *Neurocomputing*, 151 (2015) 1005.
20. M.X. Chai, Z.Y. Li, X.N. Song, J.H. Ren, Q.W. Cui, *Int. J. Electrochem. Sci.*, 16 (2021). doi: 10.20964/2021.09.35.
21. X. L. Fang, N. S. Qu, Y. D. Zhang, Z. Y. Xu and D. Zhu, *J. Mater. Process. Technol.*, 214 (2014) 556.
22. D. Zhu, W. Wang, X. L. Fang, N. S. Qu, and Z. Y. Xu, *CIRP Annal-Manufacturing Technology*, 59

(2010) 239.
23. Y. L. Chen, X. C. Zhou, P. X Chen and Z. Q. Wang, *Chinese. J. Aeronaut.*, 33 (2020) 1057.
24. S. Hinduja and J. Pattavanitch, *CIRP J. Manuf. Sci. Tec.*, 12 (2016) 79.